Fermi Surface Topology and Rashba-Edelstein Charge-Spin Conversion in Lead-Halide Perovskites

A. Filippetti[1,2,], P. Wadhwa[1], C. Caddeo[2], and A. Mattoni[2].*

[1] Dipartimento di Fisica, Università di Cagliari, Cittadella Universitaria, S. P. Monserrato-Sestu Km.0,700, Monserrato 09042-I (CA), Italy.

[2] Consiglio Nazionale delle Ricerche CNR-IOM Cagliari, Cittadella Universitaria, S. P. Monserrato-Sestu Km.0,700, Monserrato 09042-I (CA), Italy.

ABSTRACT

The conversion of charge current into spin current by the Rashba-Edelstein effect enables the reciprocal control of electron charge and magnetization in magnetoelectric and magneto-optical devices. We describe the fundamentals of this effect in 3D lead-halide perovskites: due to spin-momentum locking, a strong charge-spin conversion, widely tunable by the injected charge density, is envisaged. Our analysis highlights the close relationship between charge-spin conversion and the topological transition occurring from the low-density, torus-shaped Fermi surface (genus 1) to the high-density, simply connected Fermi surfaces (genus 0). At room temperature, spin-polarizations as large as ~10% are obtained for input charge currents in the ~10^2-10^6 Acm^{-2} range; at low temperature, almost full spin-polarization can be achieved, owed to the large, impurity scattering-limited mobilities. Our results qualify lead-halide perovskites as suitable materials for spin-orbitronic applications.

1. Introduction

Spin-orbitronics[1-12] is quickly becoming the most exciting frontier for magneto-electric and magneto-optical applications. The possibility to exploit spin-orbit coupling to inject and manipulate spin and charge currents in non-magnetic materials without an applied magnetic field is fostering the design of visionary devices with superior performances in terms of low energy consumption, operational speed, and information storage density. However, implementing these functionalities requires materials featuring several key properties which are hard to find altogether: first and foremost, a large and robust spin-orbit coupling (SOC) for the electronic states at the band gap extrema; in addition, good electron mobility, flexibility of structural and chemical design, easy integration within 2D heterostructures and devices, and possibly low-cost growth processing. Strikingly, hybrid perovskites (HP's) have shown, over the last 10 years of rabid investigation, to virtually possess all these characteristics. Since 2014, theoretical works[13-27] have predicted the presence of a strong Rashba effect (RE)[28,29] on both valence and conduction bands of the HP's main prototypes, methylammonium lead-iodide (MAPI) and lead-bromide (MAPB), owed to the large SOC of Pb, I, or Br atoms. At the experimental level, the actual presence of RE has been subject of an intense, still ongoing controversy.[30-39] In fact, most of the results are based on indirect evidence, insofar as direct angle-resolved photoemission measurements with high *k*-space resolution are complicate for HP's. Against the RE presence is the plain fact that bulk MAPI does not present macroscopic polarization, at least at room T; nevertheless, the RE has been revealed in dynamical form in 3D perovskites due to structural fluctuations,[17-19,23-27] or in static form in 2D perovskites,[40-45] nanocrystals,[46,47] interfaces,[48,49] quantum dots,[50] and doped perovskites.[51,52]

Aside from the RE debate, the last few years have also seen a flourishing of magneto-optical experiments on HP's, mostly based on spin-selected photocurrent excitations by circularly polarized light (i.e. circular photogalvanic effect). An amazing magneto-optical phenomenology was revealed, encompassing optical spin injections and spin currents with ps-order lifetime in MAPI,[53] MAPB,[54,55] and $CsPbBr_3$,[56] spin-selective optical Stark effect in HP's thin films,[57] optically-switched magnetism in magnetically doped HP's.[58] It is very clear that the combined presence of magneto-electric and magneto-optical coupling in HP's opens the view to a vast landscape of intriguing implementations, with virtually endless possibilities in terms of structural and chemical variants.

The phenomenon of charge-spin conversion is at the fundament of spin-orbitronic devices. It can be generated by two mechanisms: the Rashba-Edelstein effect (REE),[59] also known as spin-galvanic effect, and the spin-Hall effect (SHE).[60,61] While they both originates from SOC and can appear simultaneously in the same material, they are radically distinct at fundamental level and should not be confused; in this work we will focus exclusively on the former. We point out that a popular misconception considers the REE as a purely 2D phenomenon, present in interfaces and heterostructures. In fact, any 3D material with strong SOC and a unique polarization axis can display robust REE,[62] and we will show that bulk MAPI is a case in point. We remark that, while the 2D case is extensively illustrated in literature,[63-67] here we provide, at our knowledge, the first 3D description of the REE. Our theoretical approach is not limited to MAPI; it can be applied to the other 3D HP's and to a wide class of semiconductors as well.

2. Results and Discussion

2.1 Fermi Surface Topology

While all qualitatively similar, the Rashba band structures obtained from ab-initio calculations show significant differences at quantitative level. Discrepancies stem from the fact that band energies are calculated for a specific, static atomic structure, which is largely undetermined in HP's: at room T the molecules rotate with ps frequency, thus a static structure is just a snapshot during the thermodynamic run. At low T, the structure is static but characterized by many closely competing nanodomains, through which the material can easily fluctuate.[68-70] Very importantly, the vast majority of these nanodomains are electrically polarized,[69] a crucial feature for the RE appearance (unlike the Dresselhaus effect[71] which only requires inversion-symmetry breaking). To deal with this peculiar behavior, two routes are proposed in literature: a fully dynamical approach, where the band structure is determined on-fly,[17-19,23-25,27] and a statistical approach, where the electronic properties are configurationally averaged over a relatively large number of static minima.[26,69] Here we assume the latter as our starting point, and describe the energies around the band extrema using a band model based on configurationally averaged ab-initio parameters. This electronic structure is then used to develop a Bloch-Boltzmann treatment for the calculation of electric current and spin-polarization.

Figure 1a shows typical conduction bands for a static, polarized MAPI structure (valence bands are qualitatively similar).[26] The RE splits the spin-degenerate parabolic band in two single-degenerate bands, characterized by opposite spin chirality in *k*-space: a clockwise (*c*) and an anticlockwise (*a*) band. According to the *k*-linear Rashba model, the band energy is:

$$\varepsilon_{c,a}\left(\mathbf{k}\right) = \frac{\hbar^2 k^2}{2m^*} \mp \alpha\, k_p \qquad (1)$$

where upper (lower) sign is for *c* (*a*) bands, α is the Rashba parameter, and $k_p = \sqrt{k_x^2 + k_y^2}$ lies in the plane perpendicular to the internal dipole field direction (hereafter assumed to be the *z* axis).

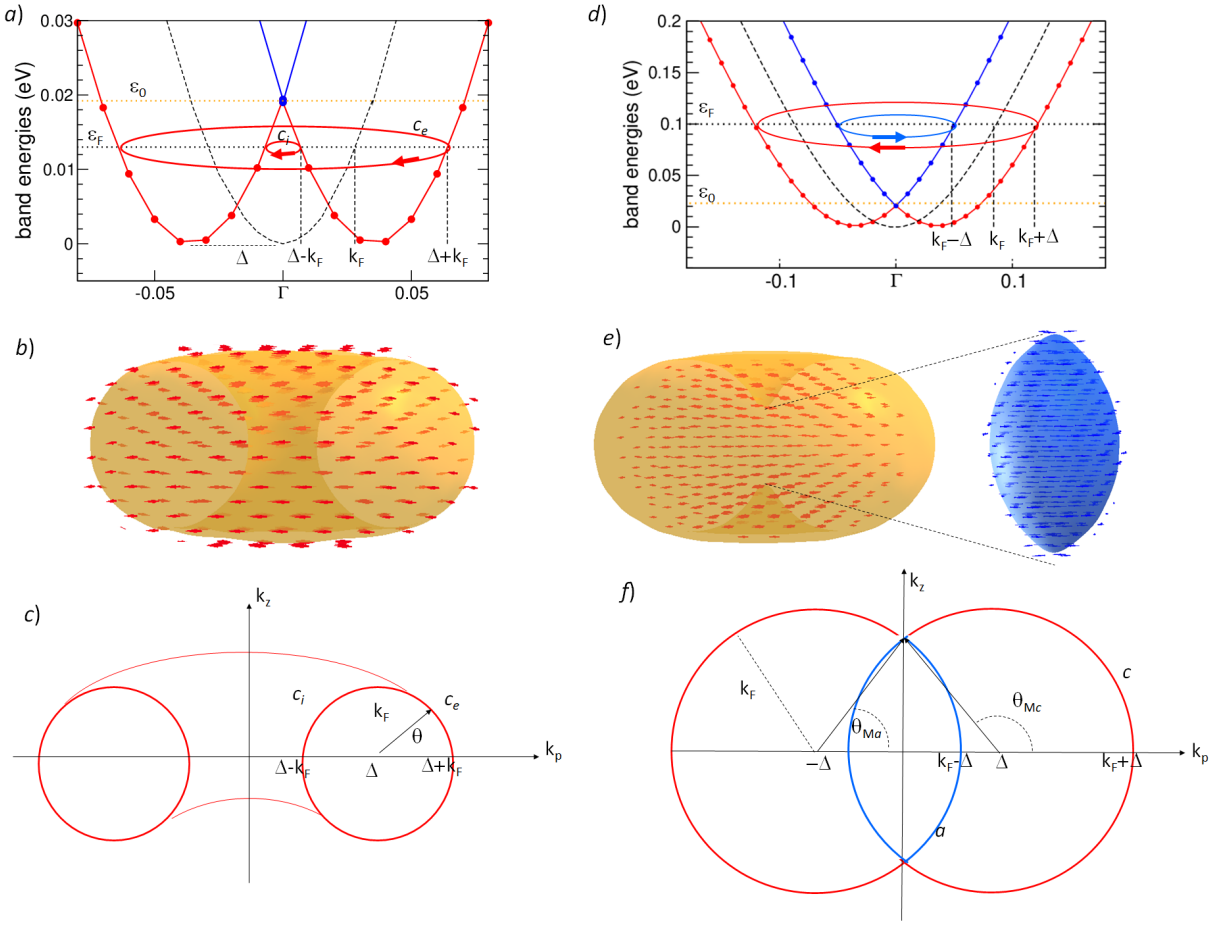

Figure 1: *a*) ab-initio calculated conduction bands of tetragonal MAPI along direction *Γ*-*X*, for $k_z = 0$; the dashed black curve indicates the double-degenerate parabolic band, red and blue curves the Rashba-split bands with opposite chirality; the orange dotted line indicate the crossing point energy ε_0 from low- to high-doping behavior, corresponding to the topological transition from toroidal to spheroidal FSs.; the arrows indicate the spin direction; Δ is the Rashba splitting in *k*-space, and k_F the Fermi vector of a Fermi sphere with equivalent ε_F. In the low-density region ($\varepsilon_F < \varepsilon_0$, $k_F < \Delta$) only the *c* band is occupied, and the FS has toroidal form. c_e and c_i circles represent external and internal side of the torus surface; at $k_z = 0$ they intercept ε_F at $\Delta+k_F$ and $\Delta-k_F$, respectively. *b*) ab-initio calculated FS of the *c* band, corresponding to a ring torus; the spin texture is indicated by the arrows. *c*): sketch of the ring torus FS with parameters used for the modeling. *d*): the same bands for electron density above the transition point ($\varepsilon_F > \varepsilon_0$, $k_F > \Delta$); in this region $k_F + \Delta$ and $k_F - \Delta$ are the Fermi vectors at $k_z = 0$ for band *c* and *a*, respectively; red and blue circles sketch the intersection of the FS's with the $k_z = 0$ plane. *e*): the ab-initio calculated FS's for bands *c* and *a*, corresponding to apple and spindle torus, respectively. *f*): sketch with parameters used to model the FS's.

This band structure preserves time reversal symmetry ($\varepsilon^{\uparrow,\downarrow}(\mathbf{k}) = \varepsilon^{\downarrow,\uparrow}(-\mathbf{k})$) but breaks inversion symmetry ($\varepsilon^{\uparrow,\downarrow}(\mathbf{k}) \neq \varepsilon^{\uparrow,\downarrow}(-\mathbf{k})$). Notice that the bottom of the energy-lowest band (*c*) is not at a single *k*-point, but it draws a circle of radius Δ. The Rashba parameter can be equivalently expressed as $\alpha = 2\varepsilon_0 / \Delta$ or $\alpha = \varepsilon_\Delta / (2\Delta)$, where ε_0 and ε_Δ are the band splitting energies at Γ and $(k_p, k_z = \Delta, 0)$, respectively. These two expressions are both used in literature, sometime generating confusion. Also, from $\partial\varepsilon_c(\mathbf{k}) / \partial k_p = 0$ we obtain $\Delta = m^*\alpha / \hbar^2 = \sqrt{2m^*\varepsilon_0} / \hbar$ and $\varepsilon_{CBB} = -\varepsilon_0$ (in Figure 1, the *c* band bottom is aligned to zero energy). Thus, the Rashba model in Equation (1) is completely defined by three parameters, m^*, Δ and ε_0 (or $\varepsilon_\Delta = 4\varepsilon_0$) which can be extracted from ab-initio band structure; vice-versa, the knowledge of α and m^* sets the values of Δ and ε_0. In our calculations we assume the following configurationally-averaged values:[26] for the conduction band α =1.2 eVÅ and m^* =0.2m_e, corresponding to $\Delta = 3.1\times10^{-2}$ Å^{-1} and ε_0 =19 meV; for the valence band α =0.7 eVÅ, m^* =0.31m_e, $\Delta = 2.8\times10^{-2}$ Å^{-1}, ε_0 =10 meV.

We are interested to evaluate the transport properties as a function of electron or hole band population; thus, a finite carrier density will be assumed, irrespectively on whether this is derived from optical excitations, electron doping, or field effect. Also, up to room T, it is a reasonable approximation to consider the contribution to transport only from carriers at the zero-temperature Fermi energy (ε_F), so that we can restrict our band analysis to the Fermi surfaces. We start from the low-doping regime defined by $\varepsilon_F < \varepsilon_0$; in this regime the *a* band is unoccupied and we can focus on the *c* band Fermi surface (FS_c), shown in Figures 1b and 1c. FS_c has the shape of a ring torus parallel to the k_z=0 plane with radius Δ; it is important to remark that the toroidal plane is always perpendicular to the direction of the dipolar field, i.e. the torus orientation is controlled

by the polarization axis. FS_c is determined by the equation $\varepsilon_c(\mathbf{k}) + \varepsilon_0 = \varepsilon_F$, where ε_0 aligns the band bottom to zero; in this way ε_F reflects the filling level distance from the band bottom. Now we define k_{Fc} as the *c*-band Fermi vector, and k_F the Fermi vector of an ε_F-equivalent Fermi sphere (to be determined later on); the FS_c equation becomes:

$$\frac{\hbar^2 k_p^2}{2m^*} + \frac{\hbar^2 k_z^2}{2m^*} - \alpha k_p + \frac{\alpha \Delta}{2} = \varepsilon_F = \frac{\hbar^2 k_F^2}{2m^*} \tag{2}$$

After elemental manipulation we obtain the general toroidal equation:

$$\frac{\left(k_p - \Delta\right)^2}{k_F^2} + \frac{k_z^2}{k_F^2} = 1 \tag{3}$$

Consider first the FS_c intercepts with the k_z=0 plane: Equation (3) allows solutions $k_P = \Delta \pm k_F$ corresponding to two circles (see Figures 1*a*, 1*c*), one internal c_i with $k_{Fc} = \Delta - k_F$, and one external c_e with $k_{Fc} = \Delta + k_F$; being on the same band, they have same spin chirality. On the (k_p, k_z) plane, Equation (3) draws the torus circular profile of radius k_F centered in (Δ, 0) (Figure 1*c*). By rotating the circle all around k_z, the whole FS_c is drawn. For a decreasing ε_F, the torus becomes thinner and thinner, up to collapsing for $\varepsilon_F = 0$ to a circle of radius Δ in the k_z=0 plane; by rising ε_F, on the other hand, the torus is progressively fattened, up to a maximum value $\varepsilon_F = \varepsilon_0$, corresponding to $k_F = \Delta$; for this value, c_i on the k_z=0 plane closes, and the two circular sections of the torus on the k_p axis touch each other. For $k_F > \Delta$, i.e. $\varepsilon_F = \varepsilon_0$, a topological phase transition occurs: the two circular sections interpenetrate into each other and progressively overlap, giving rise to two distinct FS's with opposite chirality (Figures 1*e* and 1*f*): an external,

apple-shaped FS_c, and an internal, spindle-shaped FS_a, completely wrapped into the former. FS_c intercepts the k_z=0 plane at the circle of radius $k_{Fc} = \Delta + k_F$, that is the only allowed solution of Equation (3). On the (k_p, k_z) plane, Equation (3) gives the apple contour with radius k_F centered in (Δ, 0) drawn in red in Figure 1*f*. By rotating this contour around k_z the whole FS_c is obtained. The corresponding Equation for FS_a is $\varepsilon_a(\mathbf{k}) + \varepsilon_0 = \varepsilon_F$ which after the same manipulation becomes:

$$\frac{\left(k_p + \Delta\right)^2}{k_F^2} + \frac{k_z^2}{k_F^2} = 1 \qquad (4)$$

On the (k_p, k_z) plane, Equation (4) draws the blue arc in Figure 1*f*, from which the spindle is obtained by 2π rotation around k_z. The spindle crosses the k_z =0 plane at $k_{Fa} = k_F - \Delta$, whereas at k_p = 0 apple and spindle must match at $k_z = k_F\sqrt{1-\left(\Delta / k_F\right)^2}$. In the view of integrating the Boltzmann Transport Equation, it is convenient to parametrize the FS contours in the (k_p, k_z) plane in terms of the circular coordinates $k_p = k_F \cos\theta \pm \Delta$, $k_z = k_F \sin\theta$, where upper (lower) sign is for FS_c (FS_a); this parametrization is valid in both regimes, but below the transition $\theta \in [0, 2\pi]$, while above the transition $\theta \in [-\theta_M, +\theta_M]$, where the maximum angle θ_M for the two bands is obtained from $\cos\theta_{M(c,a)} = \mp\chi$, where we define $\chi = \Delta / k_F$. As χ varies from 1 to 0, θ_{Mc} goes from π to π/2, and θ_{Ma} from 0 to π/2. In the very-high density limit $\chi \ll 1$, the two circular sections of the apple progressively overlap onto each other as their center distance (2Δ) becomes less and less significant with respect to the growing radius k_F; thus, apple and spindle coalesce into a double-degenerate Fermi spheres, and the RE vanishes.

2.2 Electronic Transport properties

Now we move to calculate the electron current by Bloch-Boltzmann theory (BBT) in relaxation time approximation.[72,73] In the following we give an outline of the main formulas, leaving the detailed formulation to the SI. Assuming an external field E applied along x, the electron mobility of a single-degenerate band is:

$$\mu_{(c,a)} = -\frac{e}{8\pi^3 n_{(c,a)}} \int d\mathbf{k}\, \tau(\mathbf{k}) \frac{\partial f_0}{\partial \varepsilon_{(c,a)}} v^2_{x,(c,a)}(\mathbf{k}) \tag{5}$$

where v_x is the band velocity in the field direction, τ the electronic relaxation time, $n_{(c,a)}$ the charge density of the band, and f_0 the Fermi-Dirac function. We assume the toroidal coordinates sketched in Figure 1*c*. The integral becomes:

$$\mu_{(c,a)} = \frac{e\tau}{4\pi^2 n_{(c,a)}} \int dk_z \int d\phi \int dk_p k_p\, \delta\left(\varepsilon_{(c,a)} - \varepsilon_F\right) v^2_{x,(c,a)}(\mathbf{k}) \tag{6}$$

where we took $\partial f_0 / \partial \varepsilon = -\delta(\varepsilon - \varepsilon_F)$; the delta function reduces the 2D integral over the (k_p, k_z) plane to a 1D integral in $ds = k_F d\theta$ over the FS contours. Also, we assume τ as purely energy-dependent, thus constant over the FS; straightforward calculations show that the squared velocity on the FS is:

$$v^2_{x,(c,a)} = \frac{\hbar^2 k_F^2}{m^{*2}} \cos^2\phi \cos^2\theta \tag{7}$$

Assembling all the results together, we obtain:

$$\mu_{(c,a)} = \frac{e\tau}{8\pi^2 m^* n_{(c,a)}} k_F^2 \int d\theta \left(k_F \cos\theta \pm \Delta\right)\cos^2\theta \tag{8}$$

For $k_F < \Delta$ (low-density regime) only FS$_c$ is present; we can solve the integral analytically:

$$\mu_c = \frac{e\tau k_F^2 \Delta}{8\pi m^* n_c} \tag{9}$$

We can evaluate k_F from the electron density in the toroidal volume:

$$n_c = \frac{1}{8\pi^3}\int d\mathbf{k} = \frac{k_F^2\Delta}{4\pi} \tag{10}$$

Clearly n_c corresponds to n, from which we can fix k_F. From Equation (10) we obtain $\mu_c = e\tau/2m^*$, i.e. carriers on the ring torus have half Drude mobility; since the Drude value matches the BBT result in case of parabolic band approximation, we can argue that factor 1/2 accounts for the mobility reduction determined by Rashba deformation of the Fermi sphere, i.e. it results from the toroidal topology. In fact, from Equation (7), averaging over ϕ and θ we have $\left\langle \cos^2\phi\cos^2\theta \right\rangle = 1/4$ and $\left\langle v_{x,(c,a)} \right\rangle = \hbar k_F / 2m^*$, i.e. the average band velocity on the torus surface is half the Fermi sphere value. For $k_F > \Delta$ (high-density regime) Equation (8) gives:

$$\mu_{(c,a)} = \frac{e\tau k_F^3}{4\pi^2 m^* n_{(c,a)}}\left[\left(1-\frac{\chi^2}{2}\right)\sqrt{1-\chi^2} - \frac{1}{3}\left(1-\chi^2\right)^{3/2} \pm \frac{\chi}{2}\arccos(\mp\chi)\right] \tag{11}$$

The charge density of the two bands is obtained integrating the density of states over apple and spindle volumes:

$$n_{c,a} = \frac{k_F^3}{2\pi^2}\left[\frac{1}{3}\left(1-\chi^2\right)^{3/2} + \frac{\chi^2}{2}\sqrt{1-\chi^2} \pm \frac{\chi}{2}\arccos(\mp\chi)\right] \qquad (12)$$

In this regime the total conductivity is $\sigma = \sigma_c + \sigma_a = en_c\mu_c + en_a\mu_a$ and the band-averaged mobility $\mu = \sigma / en$ with $n = n_c + n_a$; now k_F cannot be directly extracted, but it can be calculated from n by numerical recursive approach.

We emphasize the dramatic change encompassed by the mobility across the topological phase transition: in the low-density regime μ is constant and unaffected by the charge density; at the transition point (χ=1) θ_{Mc} = π/2, thus Equations (11) and (12) give $n_c = k_F^3 / 4\pi$, $n_a = 0$, and $\mu_c = e\tau / 2m^*$. In the high-density limit ($\chi \to 0$) $n_c = n_a = k_F^3 / 6\pi^2$ and $\mu_c = \mu_a = e\tau / m^*$, i.e. the effect of Rashba band deformation vanishes, and we recover the double-degenerate parabolic band behavior. Thus, in the high-density regime the mobility is k_F-dependent, and it evolves from the Rashba-distorted value at the transition point to the conventional Drude-like behavior in the very high-density limit. The strong mobility dependence on the charge density is a remarkable signature of the band deformation caused by RE.

Conductivity and mobility for MAPI are reported in **Figure 2**; a key ingredient in our formulation is the relaxation time, which includes electron scattering from charged impurities, acoustic phonons, and longitudinal optical photons.[74] The latter governs the MAPI mobility at room temperature;[74-76] the low-temperature mobility is limited by impurity scattering, which we fix at the reference level $N_{imp} = 10^{17}$ cm^{-3} most often reported in literature. In Figures 2*a* and 2*b* we report σ and μ vs n at several T, respectively; total values, as well as separate *c*-band and *a*-band values are displayed. The topological transition occurs for $n_{th} = 2.5\times10^{18}$ cm^{-3}; below the

transition, only the *c*-band contribution is present; in this regime the mobility is barely density-dependent, and the conductivity rises about linearly with *n*.

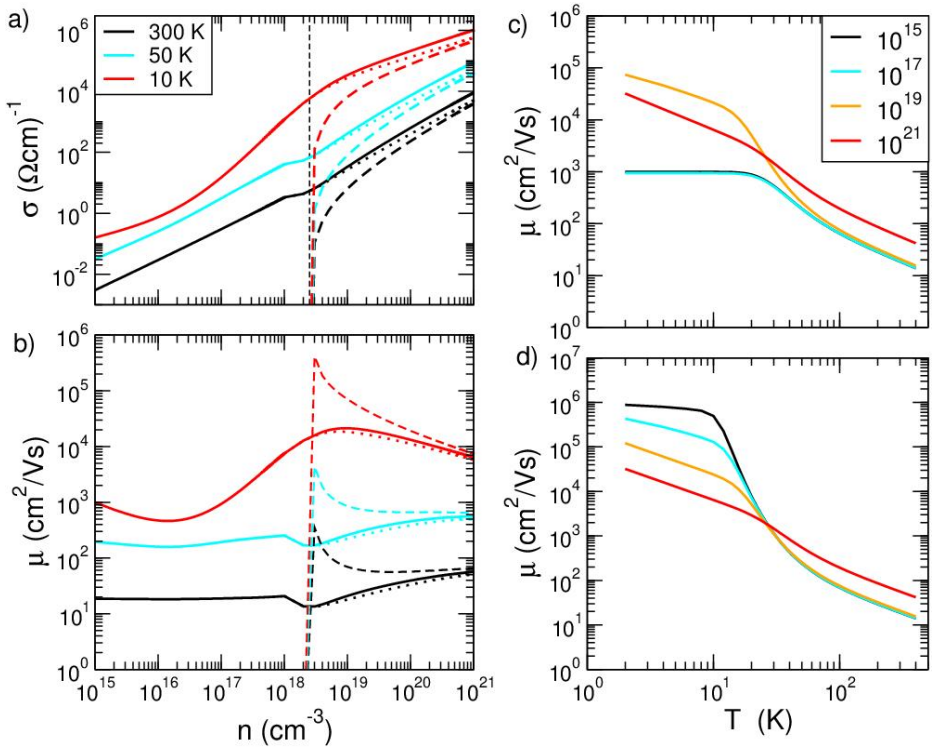

Figure 2: a) Calculated electron conductivity and b) mobility for MAPI as a function of injected conduction charge density for various temperatures, indicated in the legend of a); solid lines are for total conductivities and mobilities, dotted and dashed lines for separate for *c*-band (σ_c and μ_c) and *a*-band (σ_a and μ_a,) contributions, respectively. The vertical dashed line indicates the topological transition. c) calculated mobilities vs temperature for different charge densities, indicated in the legend in cm^{-3}. d) same as in c) but assuming a lower amount of defect concentrations (see text).

Immediately above the transition, μ_a quickly rises and peaks, owed to its Dirac-cone band shape, but since n_a is small, the *a*-band contribution to σ and μ is marginal (see the difference between solid and dotted curves). At room-T, the dominant scattering process is with the energy-lowest LO phonon, whose energy $\hbar\omega_{LO}$ = 10 meV was established by accurate calculations.[77] In Figure 2b we can see a sudden drop in mobility for n ~10^{18} cm^{-3}, which corresponds to a Fermi

level critical value $\varepsilon_F = \varepsilon_{CBB} + \hbar\omega_{LO}$: at lower densities, the carrier can only absorb the LO phonon, while at higher density it can both absorb and emit the phonons, thus undergoing an increase in scattering rate. As ε_F is progressively distanced from $\hbar\omega_{LO}$, the scattering rate decreases. Notice that the kink is still visible at 50 K, but not at 10 K, since the LO phonon scattering is overseeded by impurity scattering.

In Figure 2c we display μ vs T for several charge densities. At room-T we obtain μ ~20 cm^2/Vs , a value in the ballpark of those typically measured for MAPI;[78-81] in the low-density regime, at high T the mobility is charge-independent, while above the topological transition we see some significant increase of μ with n (e.g. μ ~60 cm^2/Vs for n =10^{21} cm^{-3}). At low T we obtain remarkably large μ values, strongly dependent on n. In order to evaluate the impact of impurity concentration, in Figure 2d we display another set of mobility results for a much lower N_{imp} = 10^{14} cm^{-3}, mimicking highly clean samples. The low-T mobilities rises by about an order of magnitude with respect to the high-impurity case, while the high-T mobilities are unchanged.

2.3 Rashba-Edelstein Charge-Spin Conversion

In 1990 Edelstein[59] pointed out that in Rashba materials the electronic current is spin-polarized, since the drifted electrons bring along the flux a net magnetization oriented perpendicularly to both current and dipole field direction (the y axis in our framework). In **Figure 3** the mechanism is illustrated on the basis of the band energy calculations reported for MAPI in ref. [26] : due to the spin-momentum locking, electrons moving along $\pm x$ experience an effective SOC field $B_{so,y} \sim \alpha k_x / \mu_B$; in equilibrium conditions this effect is compensated, but under an applied field E along, say x, the Fermi contour shifts towards $-x$ by $\delta = eE\tau/\hbar$. In the

low-density regime, only FS*c* is present (Figure 3a): the ring torus shifts towards -*x* generating a net spin accumulation along +*y*; in the high-density regime, FS*c* and FS*a* (Figures 3a and 3b) both shift towards -*x*; their spin accumulations partially compensate due to the opposite spin orientation, but the former prevails due to its larger population, thus a net magnetization along +*y* still occurs. We emphasize that the virtual totality of the REE descriptions proposed in literature assume a fixed, large charge density, with the two compensating FS's both populated. Here, on the other hand, we are interested to give a full account of the REE at variable charge density, from the very low to very high limit.

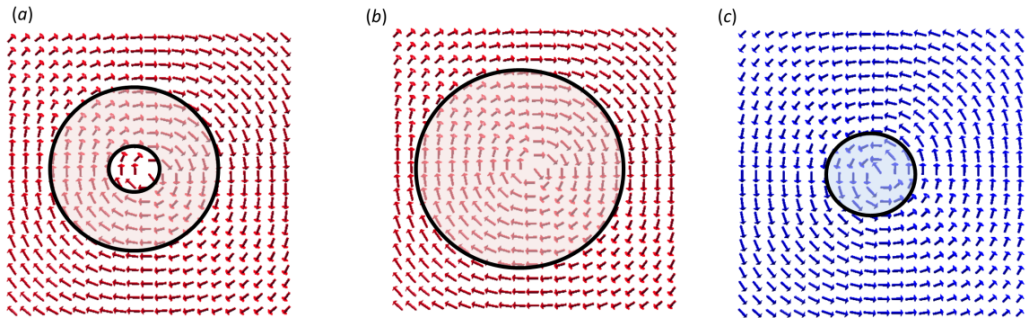

Figure 3: Spin texture of the conduction bands calculated ab-initio for MAPI inside a squared $k_z = 0$ slice of the BZ. Spins are indicated by arrows of length proportional to the spin expectation value. *a*) *c* band intersection with the ring torus FS contour appearing in the low-density regime. b) *c* band intersection with the apple torus FS contour appearing in the high-density regime. c) *a* band intersection with the spindle torus FS contour appearing in the high-density regime. The FS's are shifted to the -*x* direction by the applied electric field along +*x*

The REE is typically measured by spin-torque or spin pumping experiments in non-magnetic/ferromagnetic (NM/FM) heterostructures:[1-9] the spin-polarization of the conduction electrons generated by REE exert a spin-torque on the magnetic moments of the FM layer, thus switching the magnetization direction, as revealed by ferromagnetic resonance. The inverse REE (IREE) is also well established: a spin current, generated by spin pumping, diffuses from the FM into the Rashba material, causing a spin-unbalance at the Fermi level; to accommodate this

unbalance, the FS must shift, as shown in Figure 3, and the electron current must flow perpendicularly to the spin-polarization direction. REE and IREE have been observed in a range of different materials including metallic interfaces,[1-3,8,9] van der Waals heterostructures,[82,83] transition-metal dichalcogenides,[84] oxide heterostructures.[85,86] Strong Edelstein effects are also observed at the surfaces of topological insulators,[4-6,87-91] where the conducive surface states are Weyl cones; this band shape radically differ from the Rashba bands examined in this study, thus they are not accounted in our modeling.

For the calculation of spin-polarization we develop a formulation similar to that used for the electronic mobility: the spinor Boltzmann average over the BZ is:

$$\mathbf{S}_{(c,a)} = \frac{e\tau E}{8\pi^3 n_{(c,a)}} \int d\mathbf{k}\ \hat{\mathbf{S}}_{c,a}(\mathbf{k}) \frac{\partial f_0}{\partial \varepsilon_{(c,a)}} v_{x,(c,a)}(\mathbf{k}) \tag{13}$$

where we fix the spinor to be in the (k_x, k_y) plane :

$$\hat{\mathbf{S}}_{c,a}(\mathbf{k}) = \frac{1}{k_p}\begin{pmatrix} \pm k_y \\ \mp k_x \end{pmatrix} = \begin{pmatrix} \pm \sin\phi \\ \mp \cos\phi \end{pmatrix} \tag{14}$$

We can proceed using again toroidal coordinates. After lengthy but straightforward manipulations (reported in the SI), we arrive at the following results. For the low-density regime:

$$S_{x,c} = 0; \qquad S_{y,c} = \frac{e\tau E}{8\pi n_c \hbar} k_F^2 = \frac{\delta}{2\Delta} \tag{15}$$

Thus, the *c* band carries a positive magnetization only along *y*, i.e. it is purely transversal to the current direction; the corresponding magnetization density is $m_{y,c} = n_c S_{y,c}$. Remarkably,

Equation (15) states that the spin polarization is determined by the FS shift to Rashba radius ratio; in fact, $\delta = 2\Delta$ corresponds to shifting the whole torus onto a single half of the semi-infinite (k_x, k_y) plane; this is tantamount to have 100% spin polarization. We remark that achieving a large $\delta = eE\tau/\hbar$ requires either strong applied electric fields or long relaxation times, i.e. high mobility; a moderate α (i.e. Δ) also benefits the δ/Δ ratio. For the high-density regime:

$$S_{x,(c,a)} = 0; \qquad S_{y,(c,a)} = \pm \frac{\delta}{4\pi^2 n_{(c,a)}} k_F^2 \left(\frac{\arccos(\mp\chi)}{2} \pm \frac{\chi}{2}\sqrt{1-\chi^2} \right) \quad (16)$$

For $\chi \sim 0$, $\arccos(\chi) = +\pi/2$ (this is the only allowed solution, since $\theta \in [0, \pi]$) and $m_{(c,a)} = n_{(c,a)} S_{y,(c,a)} = \pm k_F^2 \delta / 16\pi$. Thus, at very high density, *c* and *a* contribution converge to the same but opposite value, so that their combined effect vanishes. The same occurs in the $\Delta \sim 0$ limit: the low-density regime disappears, and the *c* and *a* contributions cancel out. Finally, the net magnetization density is $m_y = n_c S_{y,c} + n_a S_{y,a}$, and the total spin-polarization fraction $S_y = m_y / n$. As shown in the SI, S_y can be interpreted as a measure of charge-spin conversion efficiency, since $S_y \sim J_s / J_c$ where J_s is the spin current generated by the unbalance of up-spin and down-spin carrier population, and J_c the total charge current.

In **Figure 4** the calculated currents and spin-polarizations vs *n* for several *T* are displayed, for the conduction bands of MAPI. To compensate for the different mobility ($\tau \sim ps$ at 10 K, ~40-60 *fs* at 50 K, ~ 3-6 *fs* at 300 K) we used increasing field values for increasing *T* (from 10^3 V/cm to 10^5 V/cm); these fields are sufficiently large to convoy a large spin-polarization S up to room T (for brevity, in the following we drop the cartesian index *y*).

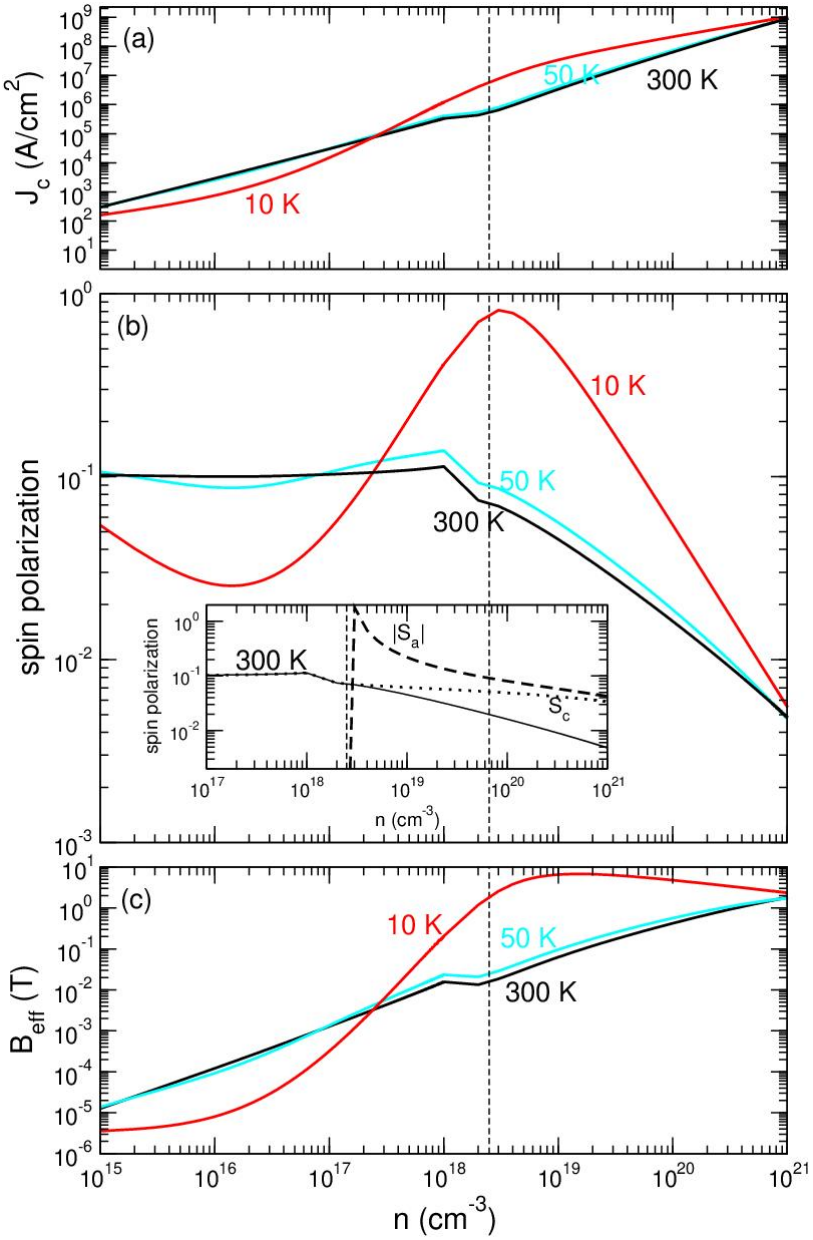

Figure 4: Calculated REE effect in the conduction bands of MAPI as a function of the injected charge densities n. Red, blue and black curves refer to 3 different temperatures, indicated in Figure. The vertical dashed line indicates the charge density threshold n_{th} corresponding to the topological transition from low- to high-density regime. a) Charge current densities. b) spin-polarization fraction S accumulated by the current flux along the $+y$ direction. Inset: solid, dotted, and dashed curves show S, S_c and $|S_a|$, respectively (S_a is negative, and differ from zero only above n_{th}). c) effective magnetic field generated by S, acting as spin-torque on the magnetization of an hypothetic magnetic semiconductor (see text).

The robustness of the charge-spin conversion can be understood by the compared analysis of current densities (Figure 4a) and the corresponding spin polarizations (Figure 4b): remarkably large S ~10% are obtained at room-T in the low charge density regime, corresponding to current densities as low as J_c ~10^2 -10^5 Acm^{-2} (a few percent S are the values measured in other Rashba systems; e.g. in Ag/Bi interfaces, S ~4% is reported).[8,9] We see that J_c is about linear with n for T=50-300 K, since for these temperatures μ is substantially independent on n ; in the same T interval, S is constant in the low-density regime, as dictated by Equation (15). For $n > n_{th}$ (n_{th} = 2.5×10^{18} cm^{-3}) we observe a relatively fast decay of S: we see (inset of Figure 4b) that S_a peaks near n_{th}, owed to the high velocity of the Dirac-like a-band; however, its negative contribution to S is discardable as long as the a band occupancy is residual; as n rises, the weight of S_a becomes more and more substantial, and S decreases up to vanishing: for n =10^{21} cm^{-3} S ~0.5%, and $S_a \approx S_c$, i.e. the spin-degenerate limit is almost recovered. At T= 10 K, owed to the very long τ , an extra-large S_y ~80% is achieved for a charge density n = 3×10^{18} cm^{-3} and a corresponding J_c ~10^7 Acm^{-2}. At low T J_c vs n visibly deviates from linearity, since τ ad μ are strongly n-dependent; for the same reason, S_c is highly n-dependent in any charge density range.

For what concern the valence bands (showed in the SI), values are similar: the slightly larger m^* and the smaller α result in a smaller Δ (and in turn n_{th} = 1.5×10^{18} cm^{-3}) for the valence; on the other hand, the conduction bands have about 30% longer τ, and in turn, larger δ ; the net result of these compensating differences is a slightly smaller S for the valence.

We remark that a direct comparison with the measurements is complicate since they are typically realized in heterostructures, not in single materials. However, we can evaluate qualitatively the spin-torque operation capabilities by an approximate expression[64-66] of the effective magnetic

field B generated by the spin-polarized currents in magnetic materials, such as, e.g. metallic ferromagnets or magnetic semiconductors: if B acts as a torque on the magnetization M of the material, it was shown that $B \simeq \left(\alpha m^* / \mu_B M\right) S J_c$. In Figure 4c we report B calculated for a reference M=10^4 A/m typical of diluted magnetic semiconductors. Within the n =10^{18} -10^{20} cm^{-3} charge density interval, we obtain J_c ~10^6 -10^8 Acm^{-2} (which are typical currents used to operate in spin-orbit torque devices), and S ~1%-10% ; these values correspond to large magnetic fields, in the range from ~0.1 T up to ~ T, thus much larger than the coercive fields (~10 mT) in these materials. To the light of the reported ferromagnetism in doped lead-halide perovskites,[92-95] our results represent a sound assessment to the possibility of exploiting magnetically-diluted, single and double perovskites for magnetic memories and magneto-optical switches.

3. Conclusions

In summary, we presented a 3D formulation of the REE-derived charge-spin conversion mechanism in MAPI at varying carrier concentration, which in our description can be equally associated to charge injection, field effect, or doping. For increasing carrier concentration, the MAPI Fermi surface undergoes a topological transformation from a ring torus with spin chirality to a couple of simply-connected closed surfaces with opposite spin chirality. This topological transition dramatically affects the electron mobility, which departs from the conventional Drude behavior. The electron mobilities plays a crucial role in the REE phenomenon: in the low-density regime ($n < n_{th}$) μ and S are simply proportional, thus they share the same linear dependence on n: at low-T the mobility in MAPI is limited by impurity scattering, and depends on the charge density, while at high-T μ is governed by polar optical phonon scattering and thus weakly

density-dependent. For the high-density regime ($n > n_{th}$), on the other hand, the behavior of μ and S with n departs, since μ increases while S decreases with n.

The optimal S is obtained by the concurrent optimization of two factors: the highest possible electron mobility, and the largest difference in the population of the two bands with opposite chirality. Our simulations show that this occurs for a carrier concentration close to the topological transition threshold $n_{th} \sim 10^{18}$ cm^{-3}; above this value, the occupancy of the two bands progressively evens, and the spin accumulation vanishes. Our results for bulk MAPI show that at room-T, $S \sim 10\%$ can be achieved for relatively modest charge currents; much larger S can be obtained at low T, owed to the much higher mobility. The favorable balance of large S (1-10%) and moderate charge currents ($J_c \sim 10^6$ -10^8 Acm^{-2}) obtained in a wide charge density interval, qualifies MAPI as a viable material for charge-spin conversion devices. We remark that our description is not restricted to MAPI but can be generally applied to any 3D Rashba material with singlet bands at the band gap extrema.

Supporting Information

Supporting Information is available from the Wiley Online Library or from the author.

Acknowledgements ???

Conflict of Interest

The authors declare no conflict of Interest

Keywords Lead-halide perovskites, electronic properties, spintronics, Rashba-Edelstein, charge-spin conversion

Bibliography

[1]I. M. Miron, G. Gaudin, S. Auffret, B. Rodmacq, A. Schuhl, S. Pizzini, J. Vogel, and P. Gambardella, Current-driven spin torque induced by the Rashba effect in a ferromagnetic metal layer. Nature Mater. **9**, 230-234 (2010).

[2]I. M. Miron, K. Garello, G. Gaudin, P.-J. Zermatten, M. V. Costache, S. Auffret, S. Bandiera, B. Rodmacq, A. Schuhl, and P. Gambardella, Perpendicular switching of a single ferromagnetic layer induced by in-plane current injection. Nature **476**, 189-194 (2011).

[3]J. C. Rojas Sanchez, L. Vila, G. Desfonds, S. Gambarelli, J.-P. Attané, J. M. De Teresa, C. Magén, and A. Fert, Spin-to-charge conversion using Rashba coupling at the interface between non-magnetic materials. Nat. Commun. **4**, 2944 (2013).

[4]L. Liu, C.-F. Pai, Y. Li, H. W. Tseng, D. C. Ralph, and R. A. Buhrman, Spin-Torque Switching with the Giant Spin Hall Effect of Tantalum. Science **336**, 555- (2012).

[5]Y. Fan, P. Upadhyaya, X. Kou, M. Lang, S. Takei, Z. Wang, J. Tang, L. He, L.-T. Chang, M. Montazeri, G. Yu,W. Jiang, T. Nie, R. N. Schwartz, Y. Tserkovnyak, and K. L. Wang, Magnetization switching through giant spin–orbit torque in a magnetically doped topological insulator heterostructure. Nature Mater. **13**, 699-704 (2014).

[6]A. R. Mellnik, J. S. Lee, A. Richardella, J. L. Grab, P. J. Mintun, M. H. Fischer, A.Vaezi, A.Manchon, E. A. Kim, N. Samarth, and D. C. Ralph, Spin-transfer torque generated by a topological Insulator. Nature **511**, 449-453 (2014).

[7]A. Manchon, H. C. Koo, J. Nitta, S. M. Frolov, and R. A. Duine, New perspectives for Rashba spin–orbit coupling. Nature Mater. **14**, 871-882 (2015).

[8]Zhang, H. J. et al. Charge-to-spin conversion and spin diffusion in Bi/Ag bilayers observed by spin-polarized positron beam. Phys. Rev. Lett. 114, 166602 (2015).

[9]H. Nakayama, Y. Kanno, H. An, T. Tashiro, S. Haku, A. Nomura, and K. Ando, Rashba-Edelstein Magnetoresistance in Metallic Heterostructures. Phys. Rev. Lett. 117, 116602 (2016).

[10]W. Han, Y. Otani, and S. Maekawa, Quantum materials for spin and charge conversion. npj Quantum Materials **3**, 27 (2018).

[11]T. Nan, C. D. Ralph, E. Y. Tsymbal, and A. Manchon, Emerging materials for spin–charge interconversion. APL Mater. **9**, 120401 (2021).

[12]L. Cheng, Z. Li, D. Zhao, and E. E. M. Chia, Studying spin–charge conversion using terahertz pulses. APL Mater. 9, 070902 (2021).

[13]M. Kim, J. Im, A. J. Freeman, J. Ihm, and H. Jin, Switchable S = 1/2 and J = 1/2 Rashba bands in ferroelectric halide perovskites. Proc. Natl. Acad. Sci. U.S.A. **111**, 6900−6904 (2014).

[14]M. Kepenekian, R. Robles, C. Katan, D, Sapori, L. Pedesseau, and J. Even, Rashba and Dresselhaus Effects in Hybrid Organic-Inorganic Perovskites: From Basics to Devices. ACS Nano **9**, 11557−11567 (2015).

[15]F. Zheng, L- Z. Tan, S, Liu, and A. M. Rappe, Rashba Spin−Orbit Coupling Enhanced Carrier Lifetime in CH3NH3PbI3. Nano Lett. **15**, 7794−7800 (2015).

[16]L. Leppert, S. E. Reyes-Lillo and J. B. Neaton. Electric Field- and Strain-Induced Rashba Effect in Hybrid Halide Perovskites. J. Phys. Chem. Lett. **7**, 3683−3689 (2016).

[17]P. Azarhoosh, S. McKechnie, J. M. Frost, A. Walsh, and M. van Schilfgaarde, Research Update: Relativistic origin of slow electron-hole recombination in hybrid halide perovskite solar cells. APL Materials **4**, 091501 (2016).

[18]T. Etienne, E. Mosconi, F. De Angelis, Dynamical Origin of the Rashba Effect in Organohalide Lead Perovskites: A Key to Suppressed Carrier Recombination in Perovskite Solar Cells? J. Phys. Chem. Lett. **7**, 1638−1645 (2016).

[19]S. Hu, H. Gao, Y. Qi, Y. Tao, Y. Li, J. R. Reimers, M. Bokdam, C. Franchini, D. Di Sante, A. Stroppa, and W. Ren, Dipole Order in Halide Perovskites: Polarization and Rashba Band Splittings. J. Phys. Chem. C **121**, 23045-23054 (2017).

[20]Z.-G. Yu, The Rashba effect and indirect electron–hole recombination in hybrid organic–inorganic perovskites. Phys. Chem. Chem. Phys. **19**, 14907 (2017).

[21]M. Kepenekian and J. Even, Rashba and Dresselhaus Couplings in Halide Perovskites: Accomplishments and Opportunities for Spintronics and Spin−Orbitronics. J. Phys. Chem. Lett. **8**, 3362−3370 (2017).

[22]S. D. Stranks and P. Plochocka, The influence of the Rashba effect. Nature Mater. **17**, 377–384 (2018).

[23]S. McKechnie, J. M. Frost, D. Pashov, P. Azarhoosh, A. Walsh, and M. van Schilfgaarde, Dynamic symmetry breaking and spin splitting in metal halide perovskites. Phys. Rev. B **98**, 085108 (2018).

[24]X. Zhang, J.-X. Shen, W. Wang, and C. G. Van de Walle, First-Principles Analysis of Radiative Recombination in Lead-Halide Perovskites. ACS Energy Lett. **3**, 10, 2329–2334 (2018).

[25]X. Zhang, J.-X. Shen, and C. G. Van de Walle, Three-Dimensional Spin Texture in Hybrid Perovskites and Its Impact on Optical Transitions. J. Phys. Chem. Lett, **9**, 11, 2903-2908 (2018).

[26]A. Filippetti, C. Caddeo, A. Bosin, P. Delugas, and A. Mattoni, Donuts and Spin Vortices at the Fermi Surfaces of Hybrid Lead-Iodide CH3NH3PbI3 Perovskites J. Phys. Chem. C **123**, 6753−6762 (2019).

[27]A. Marronnier, G. Roma, M. A. Carignano, Y. Bonnassieux, C. Katan, J. Even, E. Mosconi, and F. De Angelis, Influence of Disorder and Anharmonic Fluctuations on the Dynamical Rashba Effect in Purely Inorganic Lead-Halide Perovskites. J. Phys. Chem. C **123**, 291−298 (2019).

[28]E. I. Rashba, Phys. Solid State. **2**, (1960) 1224–1238 (1960).

[29]Y.A. Bychkov and E. I. Rashba, J. Phys. C: Solid State Phys. **17**, 6039–45 (1984).

[30]D. Niesner, M. Wilhelm, I. Levchuk, A. Osvet, S. Shrestha, M. Batentschuk, C. Brabec, and T. Fauster, T. Giant Rashba Splitting in CH3NH3PbBr3 Organic-Inorganic Perovskite, Phys. Rev. Lett. **117**, 126401 (2016).

[31]E. M. Hutter, M. C. Gélvez-Rueda, A. Osherov, V. Bulovic, F. C. Grozema, S. D. Stranks and T. J. Savenije, Direct–indirect character of the bandgap in methylammonium lead iodide perovskite. Nat. Mater. **16**, 115–120 (2017).

[32]T. Wang, B. Daiber, J. M. Frost, S. A. Mann, E. C. Garnett, A, Walsh, and B. Ehrler. Indirect to direct bandgap transition in methylammonium lead halide perovskite. Energy Environ. Sci. **10**, 509-515 (2017).

[33]V. Sarritzu, N. Sestu, D. Marongiu, X. Chang, Q. Wang, S. Masi, S. Colella, A. Rizzo, A. Gocalinska, E. Pelucchi, M. L. Mercuri, F. Quochi, M. Saba, A. Mura, and G. Bongiovanni, Direct or Indirect Bandgap in Hybrid Lead Halide Perovskites? Adv. Optical Mater. **6**, 1701254 (2018).

[34]J. M. Richter, K. Chen, A. Sadhanala, J. Butkus, J. P. H. Rivett, R. H. Friend, B. Monserrat, J. M. Hodgkiss, and F. Deschler, Direct Bandgap Behavior in Rashba-Type Metal Halide Perovskites. Adv. Mater. **30**, 1803379 (2018).

[35]K. Frohna, T. Deshpande, J. Harter, W. Peng, B. A. Barker, J. B. Neaton, S. G. Louie, O. M. Bakr, D. Hsieh, and M. Bernardi, Inversion symmetry and bulk Rashba effect in methylammonium lead iodide perovskite single crystals Nature Commun. **9**, 1829 (2018).

[36]M. Sajedi , M. Krivenkov , D. Marchenko , A. Varykhalov , J. Sánchez-Barriga, E. D. L. Rienks , and O. Rader, Absence of a giant Rashba effect in the valence band of lead halide perovskites. Phys. Rev. B **102**, 081116(R) (2020)

[37]D. Niesner, M. Hauck, S. Shrestha, I. Levchuk, G. J. Matt, A. Osvet, M. Batentschuk, C. Brabecc, H. B. Weber, and T. Fauster, Structural fluctuations cause spin-split states in tetragonal (CH3NH3)PbI3 as evidenced by the circular photogalvanic effect Proc. Natl. Acad. Sci. **115**, 9509–9514 (2018).

[38]Z. Liu, C. Vaswani, X. Yang, X. Zhao, Y. Yao, Z. Song, D. Cheng, Y. Shi, L. Luo, D.-H. Mudiyanselage, C. Huang, J.-M. Park, R. H. J. Kim, J. Zhao, Y. Yan, K.-M. Ho, and J. Wang, Ultrafast Control of Excitonic Rashba Fine Structure by Phonon Coherence in the Metal Halide Perovskite CH3NH3PbI3. Phys. Rev. Lett. **124**, 157401 (2020).

[39]E. Lafalce, E. Amerling, Z.-G. Yu, P. C. Sercel, L. Whittaker-Brooks, and Z. V. Vardeny, Rashba splitting in organic–inorganic lead–halide perovskites revealed through two-photon absorption spectroscopy. Nature Commun. **13**, 483 (2022).

[40]Y. Zhai, S. Baniya, C. Zhang, J. Li, P. Haney, C.-X. Sheng, E. Ehrenfreund, Z. V. Vardeny, Giant Rashba splitting in 2D organic-inorganic halide perovskites measured by transient spectroscopies. Sci. Adv. **3**, e1700704 (2017).

[41]J. Yin, P. Maity, L. Xu, A. M. El-Zohry, H. Li, O. M. Bakr, J.-L. Brédas, and O. F. Mohammed, Layer-Dependent Rashba Band Splitting in 2D Hybrid Perovskites. Chem. Mater. **30**, 8538−8545 (2018).

[42]I.-H. Park, Q. Zhang, K. C. Kwon, Z. Zhu, W. Yu, K. Leng, D. Giovanni, H. S. Choi, I. Abdelwahab, Q.-H. Xu, T. C. Sum, and K. P. Loh, Ferroelectricity and Rashba Effect in a Two-Dimensional Dion-Jacobson Hybrid Organic−Inorganic PerovskiteJ. Am. Chem. Soc. **141**, 15972−15976 (2019).

[43]S. B. Todd, D. B. Riley, A. Binai-Motlagh, C. Clegg, A. Ramachandran, S. A. March, J. M. Hoffman, I. G. Hill, C. C. Stoumpos, M. G. Kanatzidis, Z.-G. Yu, and K. C. Hall, Detection of Rashba spin splitting in 2D organic-inorganic perovskite via precessional carrier spin relaxation. APL Mater. **7**, 081116 (2019).

[44]X. Liu, A. Chanana, U. Huynh, F. Xue, P. Haney, S. Blair, X. Jiang, and Z.V. Vardeny, Circular photogalvanic spectroscopy of Rashba splitting in 2D hybrid organic–inorganic perovskite multiple quantum wells. Nat. Commun. **11**, 323 (2020).

[45]M. T . Pham, E. Amerling, H. M. Luong, H. T. Pham, G. K. Larsen, L. Whittaker-Brooks, and T. D. Nguyen, Origin of Rashba Spin-Orbit Coupling in 2D and 3D Lead Iodide Perovskites. Sci. Rep. **10**, 4964 (2020).

[46]Y. D. Glinka, R. Cai, J. Li, T. He, and X. W. Sun, Observing dynamic and static Rashba effects in a thin layer of 3D hybrid perovskite nanocrystals using transient absorption spectroscopy. AIP Advances **10**, 105034 (2020).

[47]M. Isarov, L. Z. Tan, M. I. Bodnarchuk, M. V. Kovalenko, A. M. Rappe, and E. Lifshitz, Rashba Effect in a Single Colloidal CsPbBr3 Perovskite Nanocrystal Detected by Magneto-Optical Measurements. Nano Lett. **17**, 5020−5026 (2017)

[48]M. Li, L. Li, R. Mukherjee, K. Wang, Q. Liu, Q. Zou, H. Xu, J. Tisdale, Z. Gai, I. N. Ivanov, D. Mandrus, and B. Hu, Magnetodielectric Response from Spin–Orbital Interaction Occurring at Interface of Ferromagnetic Co and Organometal Halide Perovskite Layers via Rashba Effect. Adv. Mater. **29**, 1603667 (2017).

[49]C. W. Myung, S. Javaid, K. S. Kim, and G. Lee, Rashba−Dresselhaus Effect in Inorganic/Organic Lead Iodide Perovskite Interfaces. ACS Energy Lett. **3**, 1294−1300 (2018).